UC San Diego
UC San Diego Previously Published Works

Title
Time-dependent modeling of dust outburst into tokamak divertor plasma

Permalink
https://escholarship.org/uc/item/22w3c37n

Journal
Physics of Plasmas, 27(8)

ISSN
1070-664X

Authors
Smirnov, RD
Krasheninnikov, SI

Publication Date
2020-08-01

DOI
10.1063/5.0009767

Copyright Information
This work is made available under the terms of a Creative Commons Attribution-NonCommercial-NoDerivatives License, available at
https://creativecommons.org/licenses/by-nc-nd/4.0/

Peer reviewed

eScholarship.org Powered by the California Digital Library
University of California

PLEASE CITE THIS ARTICLE AS DOI: 10.1063/5.0009767

Time-dependent modeling of dust outburst into tokamak divertor plasma

R.D. Smirnov[1, a)] and S.I. Krasheninnikov[1]
Department of Mechanical and Aerospace Engineering, University of California San Diego,
La Jolla CA, 92093

(Dated: 22 July 2020)

The first self-consistent simulation studies of impact of transient injection of tungsten dust on ITER-like edge plasma are presented. The simulations are performed using DUSTT and UEDGE codes coupled in fully time-dependent manner. The evolution of the divertor and upstream plasma conditions, following the injection of tungsten dust of various quantities and sizes at the outer strike point, is investigated. The estimates of the core plasma impurity fraction and the core impurity screening factor associated with the dust injection are also obtained. The simulations show that the bursts of even modest amounts of tungsten dust injected into the divertor plasmas can result in large perturbations of the divertor power load and unacceptable levels of the core plasma contamination with tungsten impurities.

I. INTRODUCTION

Magnetic fusion energy generation would require producing burning D-T plasma discharges for time periods much exceeding present fusion experiments. It is expected that plasma conditions with net positive fusion energy output $Q \sim 10$ for intervals of several minutes will be demonstrated on ITER tokamak[1]. For an extended fusion plasma operation the issues related to dust forming inside the vacuum chamber and entering the plasma become of importance. From nano- to millimeter size dust grains and droplets can be produced in tokamaks due to damage of plasma-facing components (PFCs) by high particle and heat fluxes, which can cause cracking, delamination, and melting of PFC materials[2]. At present, it is generally understood that the dust can be a significant source of impurities in fusion plasmas, as the macroscopic size dust grains contain large quantities of material and are not confined by the magnetic field due to their extremely small charge-to-mass ratio. But unlike PFC material sputtering by plasma particles, dust-related impurity sources in tokamaks are rather irregular and less predictable. Recent experimental campaigns on Large Helical Device (LHD) with 1-3 MW heating power L-mode plasma discharges, each exceeding 1000 seconds in duration, demonstrated that accidental ejection of dust from PFCs into the plasma was a main cause of termination of the discharges, preventing achieving an hour mark[3]. The sources of dust in LHD varied and included pealing of deposited layers from ICRF antenna shield and divertor surfaces, localized melting of in-vessel components, and wall damage by unipolar arcs. These processes are likely to exacerbate with increased power and duration of discharges in future fusion devices.

Studies of dust related phenomena in fusion devices relatively recently attracted substantial attention and at present are being actively pursued. Among aspects critically important for understanding of dust impact on performance of fusion devices are dust transport and interactions with fusion plasmas. Currently, dust related studies are performed on all major tokamaks and include both experimental observations and modeling of dust dynamics in fusion plasmas[2–15]. Several codes have been developed for modeling of dust transport in tokamas including DUSTT[16,17], DTOKS[18], MIGRAINe[19], DUSTTRACK[20]. Such codes can simulate trajectories of dust grains in fusion plasma, taking into account dust charging, acceleration, heating, and ablation by plasma particles, and provide dust-related impurity sources to fluid plasma transport codes employing Monte-Carlo sampled dust ensemble. Our past studies of dust impact on edge plasmas have demonstrated that dust-produced impurities can substantially increase radiative plasma cooling affecting edge conditions and even inducing thermal plasma collapse[21–23]. However, these studies were limited to steady-state conditions, where dust-originated impurity sources have been assumed stationary. This assumption, however, can be satisfied only for dust continuously injected into plasma, for example, in dust dropper experiments for wall conditioning purposes[24]. Production and ejection of the dust naturally occurring in tokamaks is on contrary highly irregular and can be associated either with intermittent plasma events, such as edge localized plasma modes (ELMs) or with accumulated over time damage to PFC materials. Thus, it is of interest to investigate effects of transient dust events on fusion plasmas, in particular, in divertor region where formation of dust is most likely due to the large particle and power loads to divertor target materials.

In the present work, we simulate evolution of the ITER-like core-edge, scrape-off-layer (SOL) and divertor plasmas following transient injection of tungsten dust grains from the strike point region of the outer divertor. The simulations are performed using DUSTT and UEDGE[25] codes coupled in fully time-dependent manner. The scale and duration of dust-induced perturbations in the plasmas are evaluated for various sizes and quantities of injected dust grains. In the following, we describe in detail the simulation model (Section II), the obtained results (Section III), provide summary of the findings and discussion of their implications for future tokamak experiments (Section IV).

II. MODEL

The edge plasma was simulated for ITER-like geometry where the 2-dimensional simulation grid covered magnetic

---

[a)] Electronic mail: rsmirnov@ucsd.edu

flux surfaces $\Psi = 0.950 - 1.035$. The indicated range of magnetic flux surfaces covers the entire SOL width and includes pedestal region of the core-edge plasma. The main plasma was assumed to be a mixture of deuterium and tritium with the average ion mass of 2.5 proton masses. The transport of neutrals in parallel to the magnetic field direction was simulated using reduced fluid model[26] and was assumed purely diffusive in the cross-field direction. Tungsten neutral and ion impurities with the charge number up to 14 were included in the simulations as individual plasma fluid species. The number of the simulated species had to be limited to achieve a reasonable compromise between the simulation performance and the model accuracy. The selected highest tungsten ion charge number approximately corresponds to effective charge of tungsten ions in corona radiative model in electron temperature range $\sim 100 - 300$ eV, where it weakly depends on the temperature[27,28]. The electron temperatures in this range and below typically correspond to the simulated ITER-like SOL plasma conditions. Neon impurities were also considered in the simulations using a fixed fraction model to reduce heat flux to the divertor targets. The fixed fraction model only considers radiation power losses from neon and does not simulate neon impurity transport in plasma. The simulated neon concentration as a fraction of the electron plasma density was set to 0.4% and 0.7% in the inner and outer divertor volumes, respectively. No neon presence was assumed in the SOL above the X-point.

The simulated boundary conditions at the core plasma interface assumed poloidally uniform total main plasma ion flux of $2.4 \cdot 10^{22}$ s^{-1} and the total 100 MW heat flux from the core equally partitioned between electrons and ions. The net flux of tungsten neutrals and ions through the core interface was set to zero. This condition must be satisfied for the initial steady state plasma solution, because there is no source of tungsten in the core. The additional hydrogen neutral source of $2.5 \cdot 10^{22}$ s^{-1} was set at the private flux (PF) region boundary of the outer divertor. The hydrogen gas pumping was simulated in the both divertors with albedo coefficient of 0.999 set at the bottom 0.36 m and 0.59 m segments of the inner and outer PF boundary, respectively. The density gradient scale length of 5 cm was used as the boundary condition for all ion species at the outer wall and the PF region boundary. The recycling coefficient at all walls and the divertor plates was equal 1.0 for hydrogen and 0.01 for tungsten ions, presuming that tungsten is non-recycling material. All walls and divertor target plates were assumed to be tungsten. Although, the impurity sources due to tungsten sputtering were included in the simulations, the sputtering provided very low background concentration of tungsten impurities in the plasma without tungsten dust injection. The simulated plasma radial transport was diffusive and anomalous. In order to emulate H-mode edge plasma profiles, the respective particle and heat anomalous cross-field diffusion coefficients were set at $D = 0.3$ m^{2}s^{-1} and $\chi = 1.0$ m^{2}s^{-1} in the SOL, and $D = 0.15$ m^{2}s^{-1} and $\chi = 0.1$ m^{2}s^{-1} in the core-edge region inside the separatrix. While the particle cross-field diffusion coefficients were fixed, the anomalous heat diffusion was considered in addition to the classical heat transport. The plasma drifts and currents were not simulated. The sheath heat transmission coefficients were assumed to be equal 5.0 for electrons and 2.5 for ions. A stationary plasma solution was computed first without dust, which provided a starting state for the simulations of the plasma temporal evolution following dust burst injection.

The DUSTT code used in this work is a dust particle tracing code, which simulates trajectories of dust grains in tokamak plasmas taking into account dust charging, heating, acceleration, and ablation by plasma particles, as well as dust solid-liquid phase transitions and collisions with PFCs. It can also provide statistically averaged parameters for an ensemble of simulated dust trajectories. Detailed description of the dust-plasma interaction models implemented in DUSTT, including particle, charge, momentum, and energy transfer processes, can be found in our previous publications[16,17,29,30]. The present simulations also use improved models of tungsten dust shielding by ablation cloud[31,32]. The tungsten dust grains of sizes 1, 10, and 100 micron were injected into divertor plasma from the outer strike point in a burst with the total injected W mass of 1, 10, and 100 mg. The injection dust velocities had Maxwellian distribution with the average speed of 10 m/s and had cosine angle distribution relative to the material surface normal direction. Total 20000 dust trajectories were tracked per simulation with equal initial statistical weight. The individual dust grain's injection times were randomly distributed with the probability proportional to $\sin^2(\pi\, t/\tau)$, where $\tau = 1$ ms is the burst duration, which in ball park corresponds to a typical ELM pulse duration.

The DUSTT and UEDGE codes were coupled via explicit exchange of data using the coupling time interval of 0.1 ms. The UEDGE code was run in time-dependent mode to simulate evolution of background plasma parameters starting with stored previous plasma state by solving time-dependent fluid plasma equations at each coupling time interval. The DUSTT code then uses the current plasma state to track trajectories of injected dust within the coupling time interval. The simulated dust ablation provides spatially distributed instantaneous source of tungsten impurity atoms at the end of the coupling interval, which is subsequently utilized by UEDGE for plasma simulations at the next coupling step. Unlike previous steady-state coupling scheme[21], instantaneous plasma conditions and characteristics of each dust grain (such as position, velocity, size, temperature, and charge) are stored in memory after each coupling step for continuous dust trajectory tracing on evolving plasma background. The both codes use independent, automatically adjusted internal time step to facilitate convergence of the plasma solutions and stability of dust dynamics at every coupling interval. During the simulations, snapshots of spatial plasma profiles and time evolution of various local and volume integrated plasma and dust parameters are recorded.

III. RESULTS

A. Initial plasma background

The radial plasma profiles prior to the dust injection as functions of the normalized magnetic flux are shown in Fig. 1. In Fig. 1(a) the electron temperature profiles at the outer mid-plane (OMP) and across the inner and outer divertor targets are plotted. The mid-plane profile shows the electron temperature of ∼ 4.8 keV and ∼ 580 eV at the core-edge interface and the separatrix, respectively. The profile has a pedestal at the separatrix that is characteristic to H-mode confinement regimes. The electron temperatures at the peak heat flux locations on the inner and outer divertor targets are ∼ 3 eV and ∼ 11 eV, respectively, Fig 1(c). This indicates the inner divertor being in semi-detached and the outer in attached regimes. The corresponding peak power fluxes, including radiative heating, are ∼ 4 $\mathrm{MW/m^2}$ and ∼ 19 $\mathrm{MW/m^2}$ to the inner and outer divertor target plates, respectively, Fig 1(b). The radial electron density profiles are shown in Fig. 1(c), where the density is $\sim 2.7\cdot 10^{19}\ \mathrm{m^{-3}}$ at the OMP separatrix location. Despite the factor 2 difference in the used plasma radial diffusion coefficients in the core-edge and SOL regions, the radial gradient of the density at the separatrix is almost absent. The radial profile of the tungsten impurity density fraction at the outer mid-plane is plotted in Fig. 1(d). The profile monotonically decreases toward the core, reaching tungsten density fraction value of $\sim 10^{-5}$ at the core interface. This value, however, does not represent an average core plasma tungsten fraction, as the core region was not simulated. These plasma conditions, consistent with the ITER expectations[33], will be used in the following sections for evaluation of magnitude of perturbations introduced by dust injection.

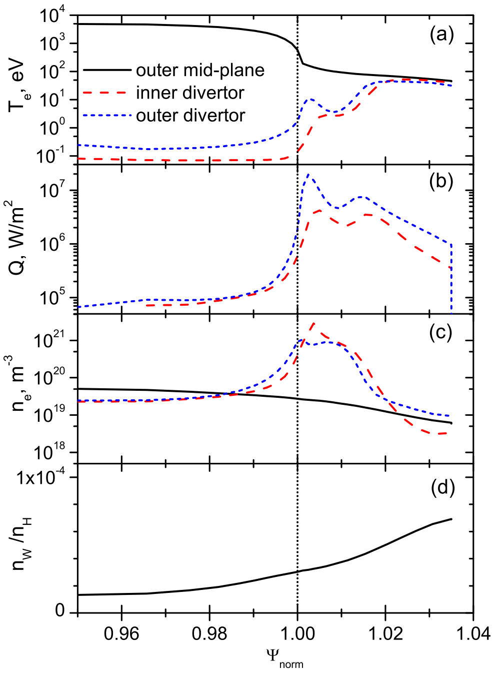

FIG. 1. Initial radial profiles of (a) electron temperature, (b) power flux at the divertor target plates, (c) electron density, and (d) tungsten impurity density fraction as functions of the normalized magnetic flux.

B. Evolution of impurity source from dust

The time evolution of volume integrated tungsten impurity sources produced by dust ablation in the plasma are shown in Fig. 2 for the different total injected quantities and sizes of the dust grains. The plotted evolution of the sources generally has a rising front, followed by a plateau and a falling front. One can see in Fig. 2 that the curves corresponding to the same dust sizes but the different quantities of injected dust have similar temporal characteristics. Such, the duration of the three stages depends mostly on the dust size and less on injected dust amount. The shape of source's rising front approximately follows the prescribed temporal profile of the dust injection. As the ablating surface of smaller dust grains is comparatively large for a given dust mass, the impurity source for the smaller dust rises more rapidly and reaches a higher plateau level than for the larger grains. It leads to the duration of the source rising front being longer for the larger dust and approaching the injection burst duration of 1 ms for the dust size of 100 μm.

The plateau stage extends to times considerably longer than the burst duration for grains larger than 1 μm and is longer for the larger grains. This can be understood, considering that dust life-time in a given plasma is ultimately dependent on its size. There are large spikes of the integrated source during the plateau phase attributable to individual grains rapidly ablating in the hot and dense plasma near the separatrix. As most of the dust ablates during the plateau, the product of the plateau level and its duration is in ball park equal to quantity of dust material assimilated in the plasma. Thus, the plateau level generally increases with the injected dust amount for a given dust size. However, the increase is weaker than linear proportionality due to reduced dust assimilation, discussed below, and slightly longer plateau phase for the higher injected dust amounts. The plateau phase duration can be roughly estimated from Fig. 2 as ∼ 1 ms, ∼ 2 − 3 ms, and ∼ 10 − 20 ms for 1, 10, and 100 μm dust, respectively. One can see that dependence of the duration of the impurity source plateau on the dust size is also weaker than linear. This is because dust grain ablation takes place along its trajectory in non-homogeneous plasma, so that larger dust grains can reach hotter plasmas where ablation rate is higher.

In Fig. 2, it can also be seen that the falling stage of the source evolution also gets longer with increase of the injected dust mass. Such dependencies of the duration of the different phases of the impurity source evolution on the amount can be

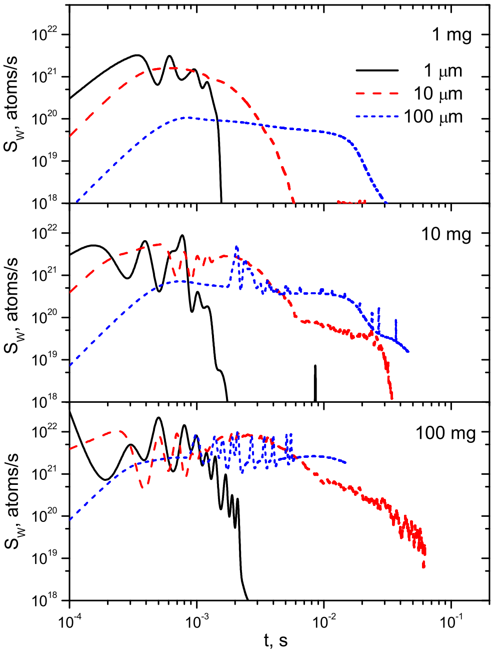

FIG. 2. Time evolution of the volume integrated source of tungsten impurity atoms from dust ablation for the different sizes and quantities of the injected dust.

explained by impact of the ablated from dust tungsten impurities on the divertor plasma conditions. As will be discussed in section III.C, large injected dust quantities lead to divertor plasma detachment and subsequently to slower ablation of the dust grains.

There are notable oscillations of the ablated impurity source plotted in Fig. 2 for 1 μm dust, as well as for larger dust grains when higher dust quantities are injected. These oscillations are accompanied by synchronous variations of plasma density and temperature in the vicinity of the dust injection location. Such localized divertor plasma oscillations, produced when sufficient amounts of tungsten dust are injected, were also reported in our previous studies[23] and mechanism of there generation was explained by development of radiation-condensation instability induced by tungsten radiation losses.[34]

Assimilated fraction of the dust material in plasma can be evaluated by integrating in time the impurity source data plotted in Fig. 2 and normalizing the result by the total quantity of the tungsten injected with dust. The results of these calculations are presented in Table I. It can be seen that the assimilated fraction is generally decreasing with increase of the injected dust amount, while such dependence gradually diminishes for the lager dust sizes. It can be qualitatively understood considering that significant plasma cooling by large injected dust quantifies leads to slower dust ablation and correspondingly to larger residual mass of dust grains able to redeposit to the PFCs. Also, the expanded recycling zone creates more favorable conditions for smaller dust grains to be pushed back to the divertor target by recycling plasma fluxes. On the other hand, larger dust grains are less sensitive to changes in the divertor plasma, while having higher chances to reach more remote PFC locations than the small grains for the same plasma parameters. These results show that for the simulated geometry a substantial fraction of injected dust grains is lost to PFCs facilitating dust migration.

TABLE I. Evaluated fraction of injected dust material assimilated in the plasma for the different sizes and quantities of injected dust.

	1 μm	10 μm	100 μm
1 mg	0.73	0.67	0.30
10 mg	0.33	0.35	0.30
100 mg	0.09	0.19	–[a]

[a] Simulated time is not sufficient for evaluation.

The simulated poloidal profiles of the volumetric tungsten impurity source from dust ablation are shown in Fig. 3 at the different times for the case of 1 mg of 100 μm dust injection. One can see in Fig. 3 that during first $\sim$ 10 ms, corresponding to the plateau phase of the total dust source (see Fig. 2), the dust ablation source is localized near the injection location and its propagation in poloidal plane can be attributed mostly to the initial distribution of dust injection velocities. At the end of the plateau stage, at 20 ms, the ablation profile becomes hollowed near the separatrix, where the dust grains do not survive by this time. Moreover, the dust propagation becomes apparently different in the SOL and PF regions. While dust grains, which trajectories lay in the PF, continue to spread, propagation of dust in the SOL is limited, as the grains are destroyed in hotter SOL plasma. By 30 ms, when the total impurity source from dust is declining, practically no dust survives in the SOL region, while remaining dust grains in more benign PF plasma continue to propagate toward the X-point. Notably, the plotted source evolution shows that dust is mostly confined in the divertor volume even for the largest dust size simulated. In the case of smaller dust sizes (not shown in Fig. 3), the ablation source profiles are much more localized near the injection location, as such dust survival time is much shorter and roughly corresponds to the end of the plateau stages plotted in Fig. 2.

In contrast to the localized impurity source profiles, further propagation of the introduced impurities has global character. In Fig. 4, the profiles of the total tungsten impurity density, including all the simulated charge states, in the divertor region are shown at the time moments of 1, 10, and 100 ms for the case of 10 mg of 10 μm dust injection. The corresponding profiles of the total tungsten impurity poloidal flux at the same time moments are plotted in Fig. 5. One can see in Fig. 4(a) that at the end of the dust burst at 1 ms the produced by dust ablation impurities are heavily concentrated in the divertor re-

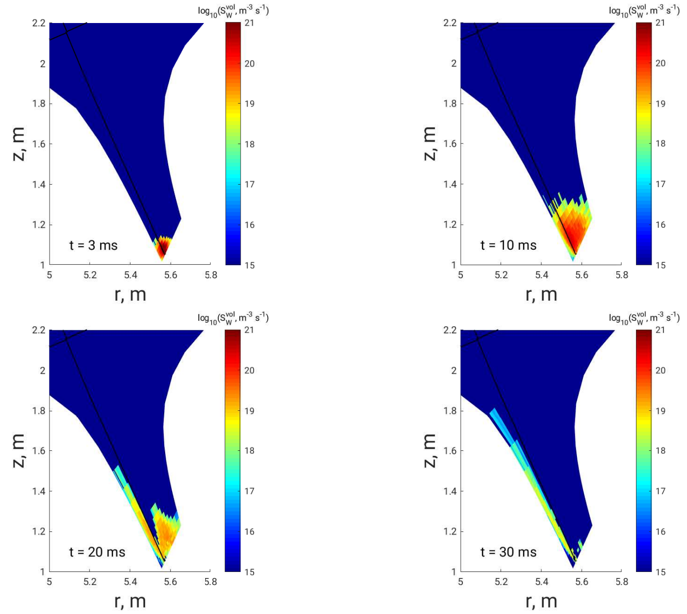

FIG. 3. The simulated evolution of poloidal profiles of tungsten impurity source provided by dust ablation in the outer divertor region at the different times for 1 mg of 100 μm dust injected.

gion near the strike point. Notably, the propagation of the impurities upstream at this early stage is faster in the mid-SOL region as compared with the near SOL, Fig. 5(a). This can be explained by the competing actions of the plasma friction and thermal forces on the ionized impurities, where the much larger plasma flux toward the target in the near SOL impedes impurity spreading. We note that there is a narrow recycling region close to strike point where the impurity flux is persistently directed toward the target plate. At 10 ms mark, which corresponds to the falling stage of the impurity source from dust, see Fig. 2, the tungsten impurities propagated through the low filed side SOL, while the upstream and the core impurity densities are significantly increased. The tungsten spreading through the SOL and divertor volume is attributed mostly to the ionized tungsten transport, as the dust grains predominantly ablate in the lower divertor part, see Fig. 3. The impurity out-flux from the divertor at this stage overtakes the near SOL, while the returning in-flux develops in region adjacent to the outer wall, Fig. 5. Such flux pattern can be attributed to the near SOL cooling by tungsten impurities and corresponding evolution of the parallel thermal force. We note that the difference between the upstream and downstream plasma temperature near the outer wall is relatively small (recall Fig. 1), so the thermal force likely does not play big role in this region. On the longer time scale of 100 ms after the beginning of the dust burst, when all the injected dust either ablated in the plasma or was lost to the walls, Fig. 4 shows depletion of the previously introduced impurities in the SOL, while significant tungsten concentrations persist in the core-edge and private flux regions. The corresponding tungsten impurity flow pattern, Fig. 5, shows substantially decreased tungsten out-flux in the near SOL and increased in-flux in the wall-adjacent SOL region. This indicates that re-deposition of the tungsten impurities preferentially takes place on the far side of the outer divertor plate. It is also interesting to note that the tungsten impurity content in the inner divertor remains elevated at 100 ms, as shown in Fig. 4.

C. Dust impact on divertor conditions

As was shown above, the dust injection leads to dramatic transient increase of the impurity concentration in the outer divertor. This in turn causes transient increase of the radiative power losses in the divertor plasma and alters divertor plasma conditions. In Fig. 6 the time evolution of the peak value of the radial profile of power flux to the outer divertor target is plotted for the different injected dust sizes and doses. The calculated power flux to the divertor targets is a sum of the plasma heat flux and the photon radiation power flux. The evolution of the power flux is largely similar between the different dust sizes for the same injected dust mass, except 10 mg of 100 μm dust case.

In the all simulated cases the peak power flux to the outer

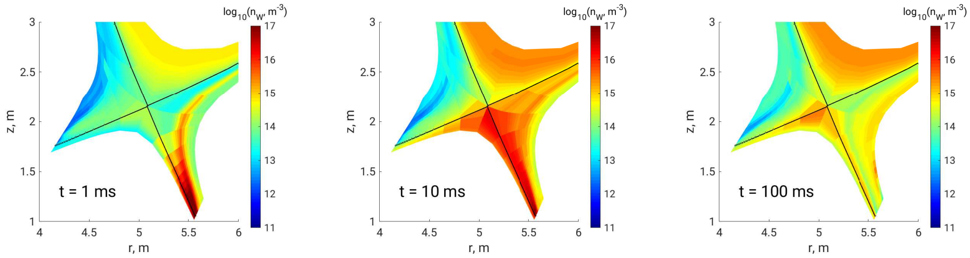

FIG. 4. The simulated profiles of tungsten impurity density in divertor region at the different times for 10 mg of 10 μm dust injected.

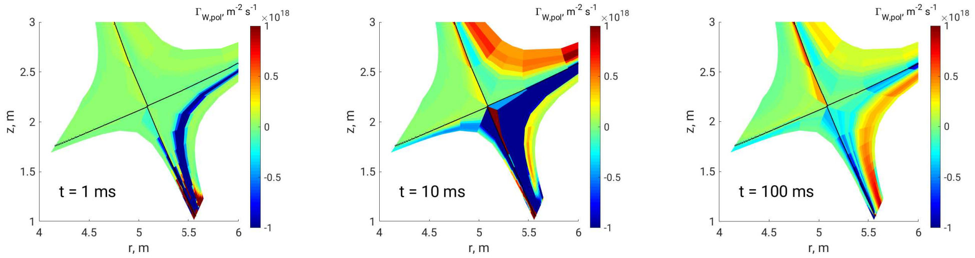

FIG. 5. The simulated profiles of tungsten impurity poloidal flux in divertor region at the different times for 10 mg of 10 μm dust injected. Positive flux corresponds to poloidal direction toward the outer divertor plate.

divertor target decreases following the dust burst. The magnitude of the decrease is generally larger for the larger injected dust quantities, while the smaller dust grains produce more rapid reduction of the flux. In the cases with dust injected mass of 1 mg (all dust sizes) and of 10 mg (1 and 10 μm), the initial drop of the power flux is followed by an increase, which substantially overshoots the initial peak power load level, e.g. in the 10 mg of 1 μm dust case the flux is about twice the initial level. Such dynamics can be described by the following complex causal sequence of plasma processes triggered by dust injection.

1. The power flux to the outer divertor target is reduced due to the radiation by both tungsten and neon impurities. The dust injection causes initially significant increase of the tungsten impurity radiation in the divertor volume (the red dashed line in Fig. 7(a))leading to less attached plasma conditions. Such conditions are characterized by the decreasing plasma temperature, accompanied by the increasing plasma density in the divertor, see the red dashed lines in Figs. 7(c,d). We note, that the volumetric radiation power of the tungsten impurities in this case remains much smaller than that of neon, Fig. 7(b), because number of neon particles in the outer divertor part of the considered flux tube is $\sim 4\cdot10^{17}$, while the maximum simulated number of tungsten particles in the same region for this case is $\sim 6\cdot10^{15}$.
2. The transient plasma density increase leads to increase of the neon impurity radiation, which is proportional to n_e^2, in most of the outer divertor volume, further reducing the power flux to the divertor target, see the red dashed line in Fig. 7(b).
3. However, on the time scale of several tens of milliseconds the tungsten impurities partially propagate upstream beyond the X-point and partially are deposited to the PFCs, causing the tungsten concentration decrease in the divertor and increase in the SOL plasma above the X-point, as was shown in section III.B.
4. Due to the high upstream plasma temperature, > 150eV, Fig. 7(c), the tungsten impurities are highly ionized there with effective impurity Z reaching the limit of 14 used in these simulations. This leads to increased ion collisionality that impedes convective parallel and enhances diffusive cross-field ion heat transport, causing the upstream plasma temperature to increase and the density to decrease along the SOL, see the green dotted lines in Figs. 7(c,d).
5. The decrease of the plasma density causes reduction of the neon radiative power losses in the divertor, leading to the increase of the divertor target power load, the green dotted line in Fig. 7(b).
6. At time of order of 100 ms after the dust injection, the tungsten concentration in the SOL plasma reduces and the plasma conditions gradually return to the pre-injection values, as illustrated by the blue dash-dotted lines in Figs. 7(a-d).

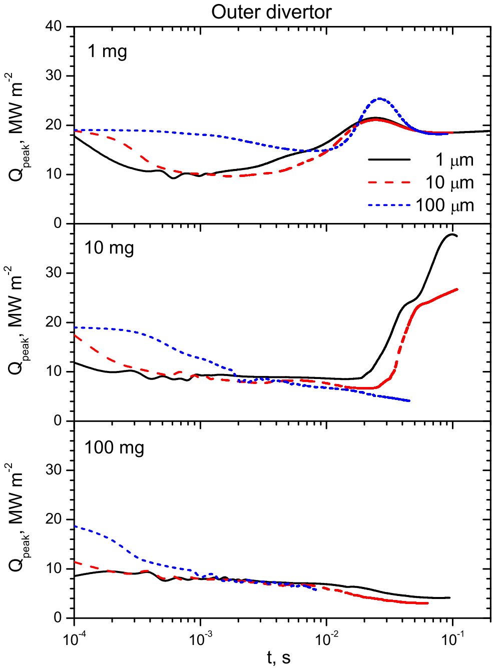

FIG. 6. Time evolution of the peak power flux to the outer divertor target plate for the different sizes and quantities of the injected dust.

As can be seen in Fig. 6, in several simulated cases with the larger injected dust doses and sizes the outer divertor power load decreases continuously during the simulated times. In these cases, unlike the ones described above, the initial cooling of the divertor plasma, induced by the tungsten dust injection, leads to detached plasma conditions, characterized by deep reduction of the divertor plasma density and temperature. Although the simulated times are not sufficiently long to see the further evolution of the divertor plasma, we can speculate that eventually the plasma state will return to the initial steady state conditions, as the simulated power and particle fluxes into the system remain constant. However, it is possible that the overshoot phase would not be observed during the recovery, because divertor plasma density is already very low in much of the divertor volume in a deeply detached state due to volumetric plasma recombination.

The evolution of the peak power flux to the inner divertor target for the simulated cases is plotted in Fig. 8. One can see comparing Figs. 4 and 7 that the dynamics of inner divertor power load is generally opposite of the outer one and is smaller in the amplitude. The counter-phase changes in the inner and outer divertors can be explained by flows of plasma particles equalizing plasma pressure between them. When the outer divertor transitions to a deep detachment, the inner divertor plasma temporarily re-attaches and the power load increases up to ~ 2 times compared to the initial value. In the 100 mg cases, the peak load is followed by reduction of the power flux below the initial one. This can be attributed to additional power losses by tungsten impurities reaching the inner divertor by this time. The cases, where the outer divertor does not transition to the deep detachment state, are characterized by the relatively small variations of the inner divertor power load.

D. Core plasma contamination

An important question related to tungsten dust outbursts is how significant the core plasma contamination by dust originated impurities is. However, because the present simulations do not include most of the core plasma volume, it is not straightforward to answer. In order to estimate tungsten content in the plasma core, we integrated in time the flux of tungsten impurities into the core from the separatrix, assuming that the radial tungsten in-flux into the core is purely diffusive with the density gradient approximately equal to the simulated tungsten density at the separatrix divided by the width of the core-edge region. Further, using the evaluated number of tungsten particles in the core and taking the core volume equal ~ 600 m^3 and the average core plasma density of $\sim 10^{20}$ m^{-3} we can estimate averaged impurity density fraction in the core plasma.

The time evolution of the evaluated fraction is plotted in Fig. 9. One can see in the figure that the core tungsten fraction is determined mostly by the injected dust mass. The role of the dust size becomes significant with the increase of the injected dust mass, when the larger core contamination is obtained for the larger dust sizes. We note that in all simulated cases the core impurity fraction increases and reaches levels above 10^{-5} and for the larger dust sizes and doses approaches and exceeds 10^{-4}. Such levels of the tungsten impurities, even when transient, can cause unacceptable radiation power losses from the core, significantly shrinking burning plasma operational window[27].

It also of interest to consider core "screening factor", calculated as the core tungsten particle content at the end of the simulations divided by the number of the tungsten atoms injected with the dust. We obtain the "screening factor" values ranging from ~ 0.03 to ~ 0.5 for the dust doses of 100 mg and 1 mg, respectively. The more effective core screening, when the larger doses of dust are injected, is in accord with the discussed in section III.B dependence of the assimilated dust material fraction on the injected dust amount. The relatively high values of the "screening factor" indicate propensity of tungsten dust to contaminate the core plasma, as the tungsten source from dust ablation is distributed in the divertor volume, providing multiple routes for tungsten impurities to penetrate the core, particularly via the private flux regions and the X-point.

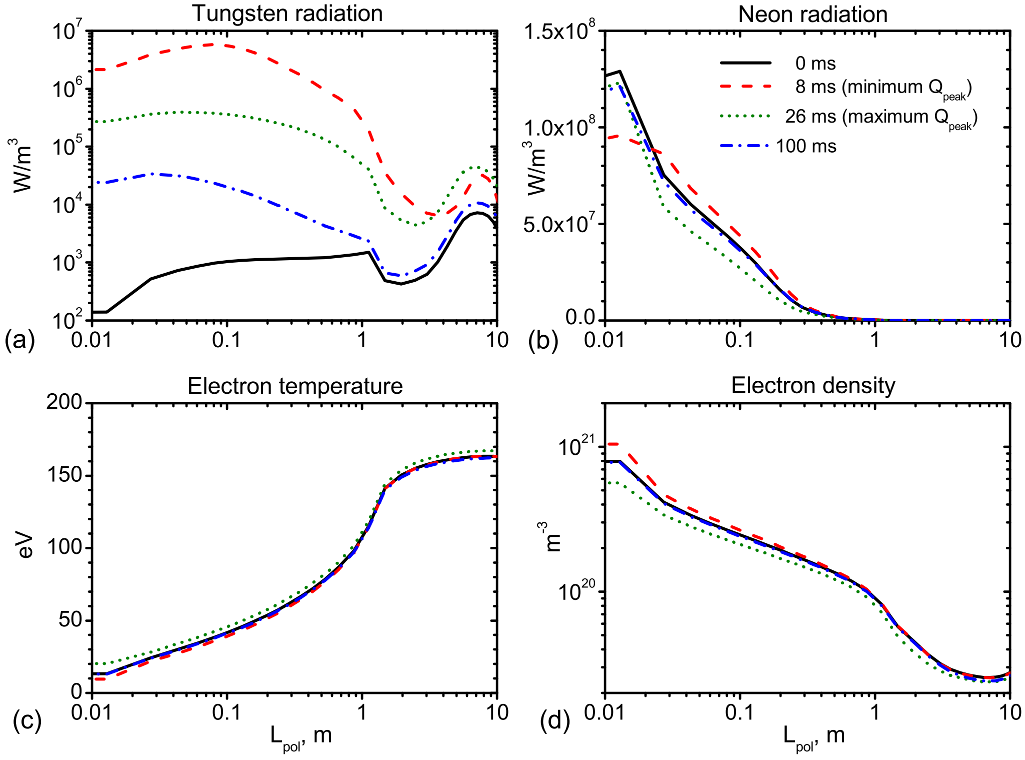

FIG. 7. Profiles of the tungsten (a) and neon (b) radiation power, the electron temperature (c) and density (d) along the magnetic flux tube, which corresponds to the maximum power flux density to the outer divertor, as functions of the poloidal distance from the divertor target plate. The profiles are shown for 1 mg of 100 μm dust injection case. The X-point position corresponds to $L_{pol} = 1.48$ m.

IV. SUMMARY AND DISCUSSION

The temporal response of ITER-like edge plasma to outburst of tungsten dust in the outer divertor region was simulated using coupled DUSTT and UEDGE codes. The simulated dust bursts of 1 ms duration and located at the outer strike point represented potential accidental ejection of tungsten caused by divertor material damage or mobilization of accumulated dust. Variety of injected dust quantities and sizes, corresponding to all combinations of 1, 10, and 100 mg and 1, 10, and 100 μm, were simulated. The simulations demonstrated that the dynamics of the tungsten impurity sources, associated with dust ablation in plasma, has a plateau phase, which duration ranges from ~ 1 ms to ~ 20 ms depending mostly on size of the injected dust. The source is localized in the divertor region, even for the largest dust size simulated. However, the transport of ionized tungsten impurities, with the thermal force playing significant role, causes their spread upstream on ~ 10 ms time scale.

Depending on the amount of dust injected, such impurity dynamics causes large transient perturbations of the divertor plasma conditions. Our simulations showed that within several milliseconds the tungsten dust injection causes large reduction of the outer divertor power load for all the simulated dust quantities. Such reduction persist for at least 100s of milliseconds when large amounts of dust, > 10 mg, are injected due to transition of the outer divertor to a deeply detached state. However, for smaller injected dust masses the initial power load reduction is followed by its significant increase, overshooting the steady-state value by a factor up to ~ 2. This phenomenon can be explained by an interplay between the power losses from the seeded neon impurity in the divertor and the changes of the upstream plasma conditions caused by increased collisionality due to transient increase of the upstream concentration of the highly ionized tungsten impurities. This unexpected result highlights complex dynamics that combination of tungsten dust injection and presence of other impurities, seeded in the divertor for power load miti-

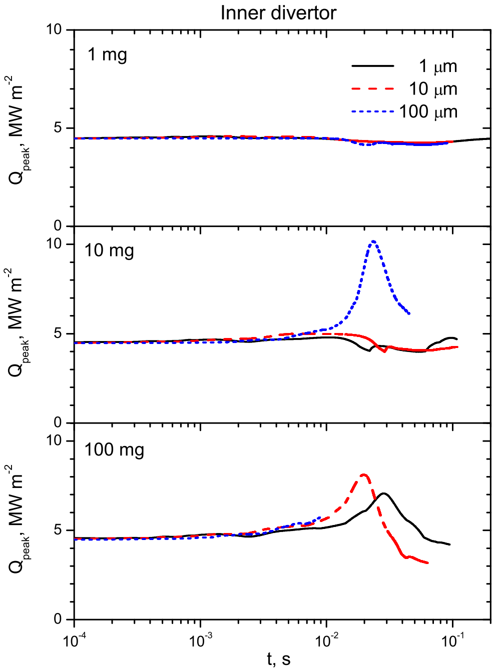

FIG. 8. Time evolution of the peak power flux to the inner divertor target plate for the different sizes and quantities of the injected dust.

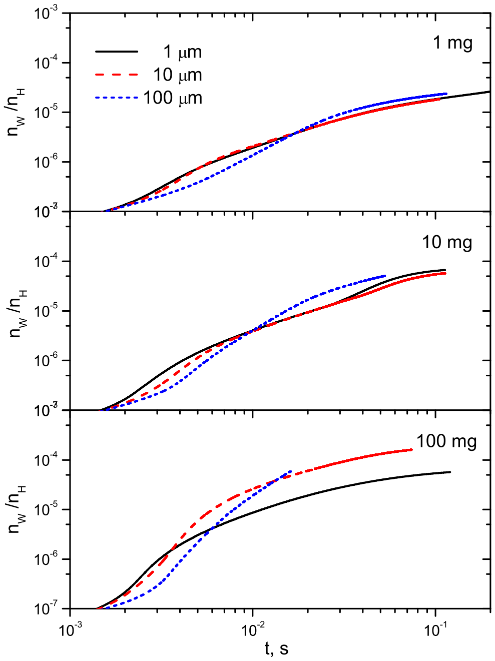

FIG. 9. Estimated averaged fraction of the tungsten impurity density in the plasma core.

gation, can produce. We also showed that the outer divertor deep detachment induced by dust causes substantial transient increase of the inner divertor power load, as its plasma becomes more attached. As the planned divertor power management in ITER will rely on maintaining semi-detached divertor plasma conditions utilizing impurity seeding, the significant perturbations of such conditions induced by an accidental dust injection should be considered.

We also estimated tungsten impurity content of the core plasma, based on the simulated upstream tungsten impurity concentrations. The estimates showed that the tungsten impurity fraction exceeds 10^{-5} level in all simulated injection cases and becomes $\sim 10^{-4}$ for injected dust masses $\sim$ 10 mg and larger. The obtained core tungsten density fraction is weakly dependent on the dust size, where the larger dust grains produce the higher impurity fractions when the large dust quantities were injected. We also evaluated core plasma "screening factor", showing that up to half of the injected tungsten mass can enter the core for 1 mg dust injection case. The factor reduces substantially for the larger dust quantities, when the dust ablation rate decreases due to the induced divertor plasma detachment. While the present results are estimates, the possibility of the substantial core contamination, even when the relatively small quantities of tungsten dust are injected transiently in the ITER divertor, should be considered.

As the presented in this paper results are the first of its kind self-consistent, time-dependent, coupled dust-plasma transport simulations, further studies of dust impact on fusion plasmas in context of future tokamaks performance are required. Such studies should include both experimental and computational efforts to extend and validate dust-plasma simulations, expand range of investigated potential dust related events in tokamaks, and provide guidelines for dust management in future fusion reactors. In particular, existing physical models of dust-plasma interactions and impurity transport in tokamaks need further benchmarking for a variety of dust parameters and plasma conditions, as such quantitative experimental data remains scarce. Furthermore, a larger number of tungsten ion charge states can be included in our future simulations to extend the considered core plasma region and provide better estimates of the core contamination with tungsten impurities. Also, the plasma drifts need to be included in further studies, as they can have important effects on tungsten impurity transport. We also note that, although DUSTT code simulates 3D dust trajectories, the toroidal plasma symmetry assumed in UEDGE does not allow to simulate 3D plasma effects related to toroidal localization of the impurity source. We plan to investigate impact of the 3D plasma transport effects in future by coupling DUSTT with BOUT++ 3D code. In addition, to provide more detailed assessment of dust impact on fusion plasmas future modeling studies need to expand scope of modeled plasma discharge conditions (e.g. magnetic configuration, heating and fueling, impurity seeding, ELMs, etc.), as well as of dust injection scenarios (e.g. dust injection location, speed, size, composition, quantity, etc.). These issues can be addressed with further improvements in performance of the codes and allocation of more computational resources to such studies. Importantly, qualitative validation of the presented in this paper and future dust modeling studies can be performed with already existing dust injection techniques on modern tokamaks.

In conclusion, it is expected that erosion of PFCs in fusion reactors can result in accumulation of very large quantities of wall material at the bottom the vessel, including in form of dust. As the presented in this paper results show, mobilization of even very small portion of such material can result in large impact on both divertor and core plasmas. This stresses the need to consider dust as a major factor in fusion performance.

ACKNOWLEDGMENTS

This material is based upon the work supported by the U.S. Department of Energy, Office of Science, Office of Fusion Energy Sciences under Award No. DE-FG02-06ER54852.

The data that support the findings of this study are available from the corresponding author upon reasonable request.

[1] ITER Organization, "ITER Research Plan within the Staged Approach (Level III – Provisional Version)," ITER technical report ITR-18-003 (ITER Organization, 2018).

[2] S. Krasheninnikov, R. Smirnov, and D. Rudakov, Plasma Phys. Control. Fusion **53**, 083001 (2011).

[3] M. Shoji, H. Kasahara, M. Tokitani, T. Seki, K. Saito, S. Kamio, R. Seki, Y. Tanaka, A. Pigarov, R. Smirnov, G. Kawamura, H. Tanaka, S. Masuzaki, Y. Uesugi, T. Mutoh, and T. L. E. Group, Nucl. Fusion **55**, 053014 (2015).

[4] D. Rudakov, A. Litnovsky, W. West, J. Yu, J. Boedo, B. Bray, S. Brezinsek, N. Brooks, M. Fenstermacher, M. Groth, E. Hollmann, A. Huber, A. Hyatt, S. Krasheninnikov, C. Lasnier, A. McLean, R. Moyer, A. Pigarov, V. Philipps, A. Pospieszczyk, R. Smirnov, J. Sharpe, W. Solomon, J. Watkins, and C. Wong, Nucl. Fusion **49**, 085022 (2009).

[5] A. Roquemore, B. John, F. Friesen, K. Hartzfeld, and D. Mansfield, Fusion Eng. Des. **86**, 1355–1358 (2011).

[6] M. Rubel, A. Widdowson, J. Grzonka, E. Fortuna-Zalesna, S. Moon, P. Petersson, N. Ashikawa, N. Asakura, D. Hamaguchi, Y. Hatano, K. Isobe, S. Masuzaki, H. Kurotaki, Y. Oya, M. Oyaidzu, M. Tokitani, and J. Contributors, Fusion Eng. Des. **136**, 579–586 (2018).

[7] F. Brochard, V. Rohde, T. Lunt, G. Suárez López, A. Shalpegin, R. Neu, and A. U. Team, Nucl. Mater. Energy **18**, 268–274 (2019).

[8] M. Balden, N. Endstrasser, P. Humrickhouse, V. Rohde, M. Rasinski, U. von Toussaint, S. Elgeti, R. Neu, and the ASDEX Upgrade Team, Nucl. Fusion **54**, 073010 (2014).

[9] A. Autricque, S. Hong, N. Fedorczak, S. Son, H. Lee, I. Song, W. Choe, and C. Grisolia, Nucl. Meter. Energy **12**, 599–604 (2017).

[10] C. Arnas, J. Irby, S. Celli, G. De Temmerman, Y. Addab, L. Couëdel, C. Grisolia, Y. Lin, C. Martin, C. Pardanaud, and S. Pierson, Nucl. Meter. Energy **11**, 12–19 (2017).

[11] A. Shalpegin, L. Vignitchouk, I. Erofeev, F. Brochard, A. Litnovsky, S. Bozhenkov, I. Bykov, N. den Harder, and G. Sergienko, Plasma Phys. Control. Fusion **57**, 125017 (2015).

[12] M. De Angeli, L. Laguardia, G. Maddaluno, E. Perelli Cippo, D. Ripamonti, M. Apicella, C. Bressan, R. Caniello, C. Conti, F. Ghezzi, G. Grosso, and G. Mazzitelli, Nucl. Fusion **55**, 123005 (2015).

[13] M. Shoji, S. Masuzaki, Y. Tanaka, A. Pigarov, R. Smirnov, G. Kawamura, Y. Uesugi, H. Yamada, and The LHD Experiment Group, J. Nucl. Mater. **463**, 861–864 (2015).

[14] N. Asakura, T. Hayashi, N. Ashikawa, and M. Fukumoto, J. Nucl. Mater. **438**, S659–S663 (2013).

[15] Z.-H. Huang, L.-W. Yan, Y. Tomita, Z. Feng, J. Cheng, W.-Y. Hong, Y.-D. Pan, Q.-W. Yang, and X.-R. Duan, Chinese Physics B **24**, 025204 (2015).

[16] A. Pigarov and S. Krasheninnikov, Phys. Plasmas **12**, 122508 (2005).

[17] R. Smirnov, A. Pigarov, M. Rosenberg, S. Krasheninnikov, and D. Mendis, Plasma Phys. Control. Fusion **49**, 347 (2007).

[18] M. Bacharis, M. Coppins, and J. Allen, Phys. Plasmas **17**, 042505 (2010).

[19] S. Ratynskaia, L. Vignitchouk, P. Tolias, I. Bykov, H. Bergsåker, A. Litnovsky, N. den Harder, and E. Lazzaro, Nucl. Fusion **53**, 123002 (2013).

[20] G. Gervasini, E. Lazzaro, and A. Uccello, J. Fusion Energy **36**, 25—39 (2017).

[21] R. Smirnov, S. Krasheninnikov, A. Pigarov, A. Roquemore, D. Mansfield, and J. Nichols, J. Nucl. Mater. **415**, S1067 (2011).

[22] R. Smirnov, S. Krasheninnikov, A. Pigarov, T. Rognlien, D. Mansfield, C. Skinner, and A. Roquemore, Contrib. Plasma Phys. **52**, 435–439 (2012).

[23] R. Smirnov, S. Krasheninnikov, A. Pigarov, and T. Rognlien, Phys. Plasmas **22**, 012506 (2015).

[24] A. Bortolon, "Real-time wall conditioning through boron powder injection in fusion devices with carbon and tungsten wall," in *Bulletin of the American Physical Society*, 61st Annual Meeting of the APS Division of Plasma Physics (October 21–25, 2019; Fort Lauderdale, Florida), Vol. 64 (2019) p. YI3.00003.

[25] T. Rognlien, J. Milovich, M. Rensink, and G. Porter, J. Nucl. Mater. **198**, 347 (1992).

[26] F. Wising, D. Knoll, S. Krasheninnikov, T. Rognlien, and D. Sigmar, Contrib. Plasma Phys. **36**, 309 (1996).

[27] T. Pütterich, R. Neu, R. Dux, A. Whiteford, M. O'Mullane, H. Summers, and the ASDEX Upgrade Team, Nucl. Fusion **50**, 025012 (2010).

[28] D. Post, R. Jensen, C. Tarter, W. Grasberger, and W.A.Lokke, At. Data Nucl. Data Tables **20**, 397 (1977).

[29] S. Krasheninnikov, T. Soboleva, Y. Tomita, R. Smirnov, and R. Janev, J. Nucl. Mater. **337–339**, 65–68 (2005).

[30] Y. Tanaka, A. Pigarov, R. Smirnov, S. Krasheninnikov, N. Ohno, and Y. Uesugi, Phys. Plasmas **14**, 052504 (2007).

[31] E. Marenkov and S. Krasheninnikov, Phys. Plasmas **21**, 123701 (2014).

[32] S. Krasheninnikov and E. Marenkov, J. Nucl. Mater. **463**, 869–872 (2015).

[33] A. Sips, G. Giruzzi, S. Ide, C. Kessel, T. Luce, J. Snipes, J. Stober, and the Integrated Operation Scenario Topical Group of the ITPA, Phys. Plasmas **22**, 021804 (2015).

[34] R. Smirnov, A. Kukushkin, S. Krasheninnikov, A. Pigarov, and T. Rognlien, Phys. Plasmas **23**, 012503 (2016).

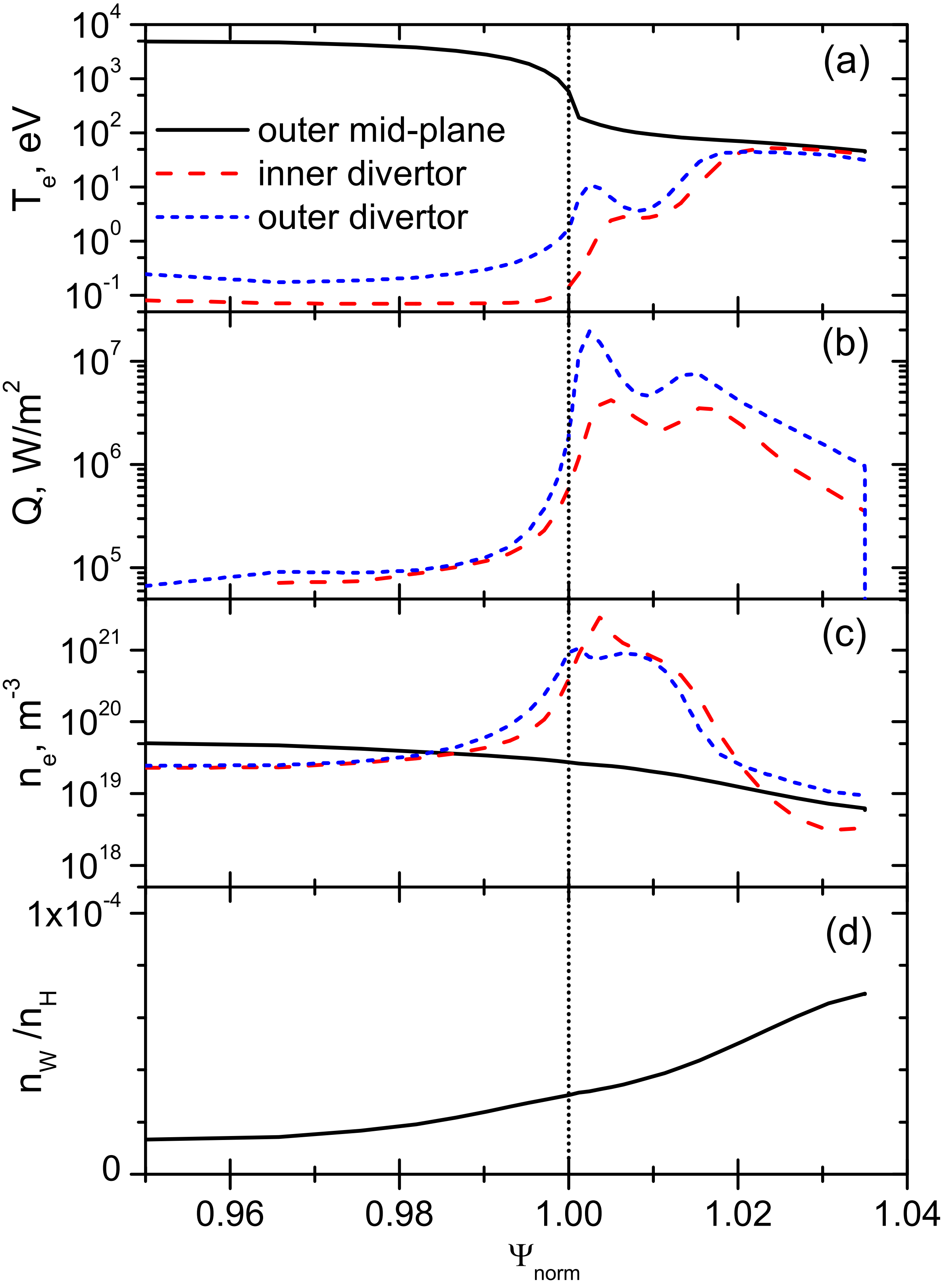
(a)
(b)
(c)
(d)
T_e, eV
Q, W/m^2
n_e, m^{-3}
n_W/n_H
outer mid-plane
inner divertor
outer divertor
10^4
10^3
10^2
10^1
10^0
10^{-1}
10^7
10^6
10^5
10^{21}
10^{20}
10^{19}
10^{18}
1×10^{-4}
0
0.96
0.98
1.00
1.02
1.04
Ψ_{norm}

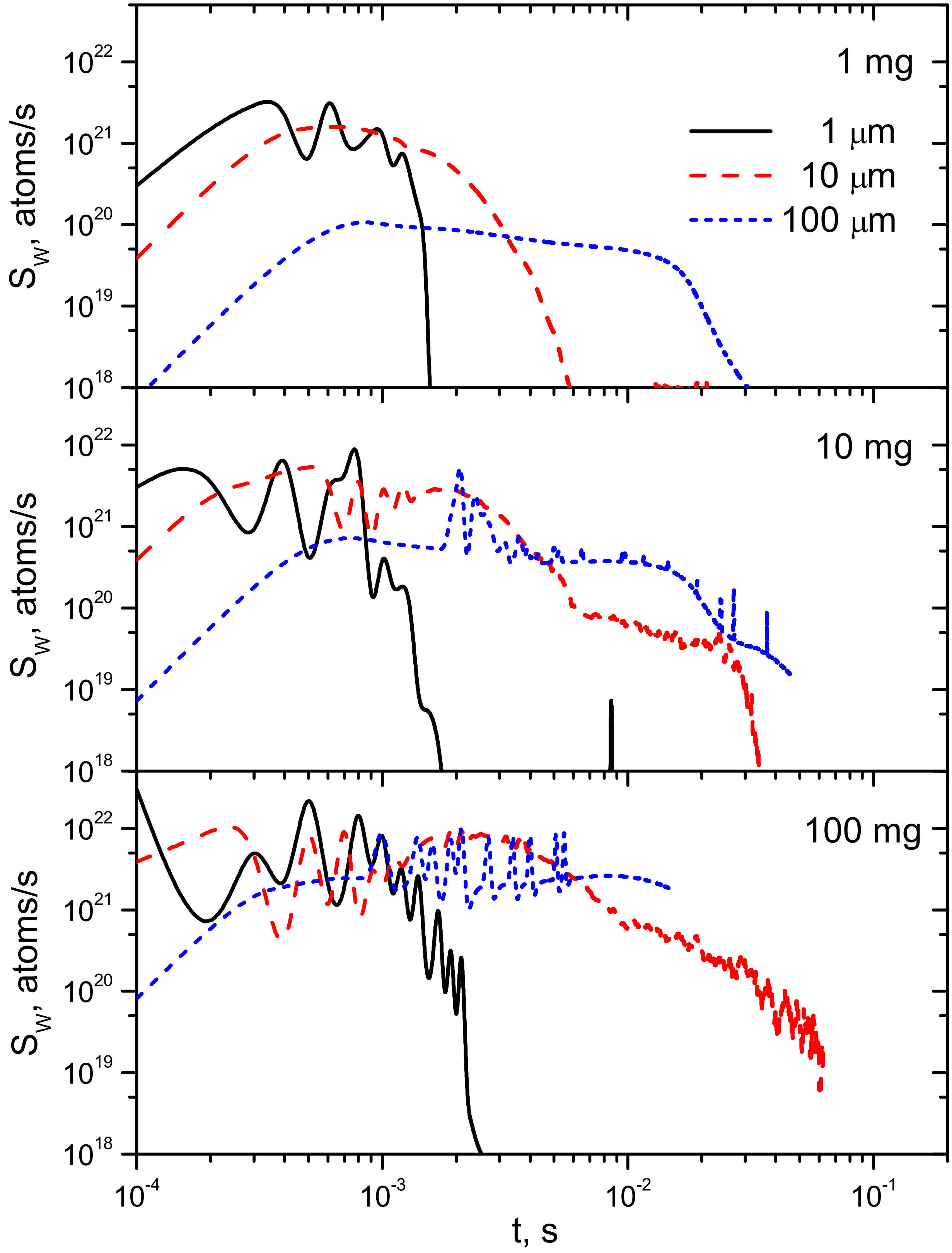
1 mg
1 μm
10 μm
100 μm
10 mg
100 mg
S_W, atoms/s
10^{18}
10^{19}
10^{20}
10^{21}
10^{22}
10^{-4}
10^{-3}
10^{-2}
10^{-1}
t, s

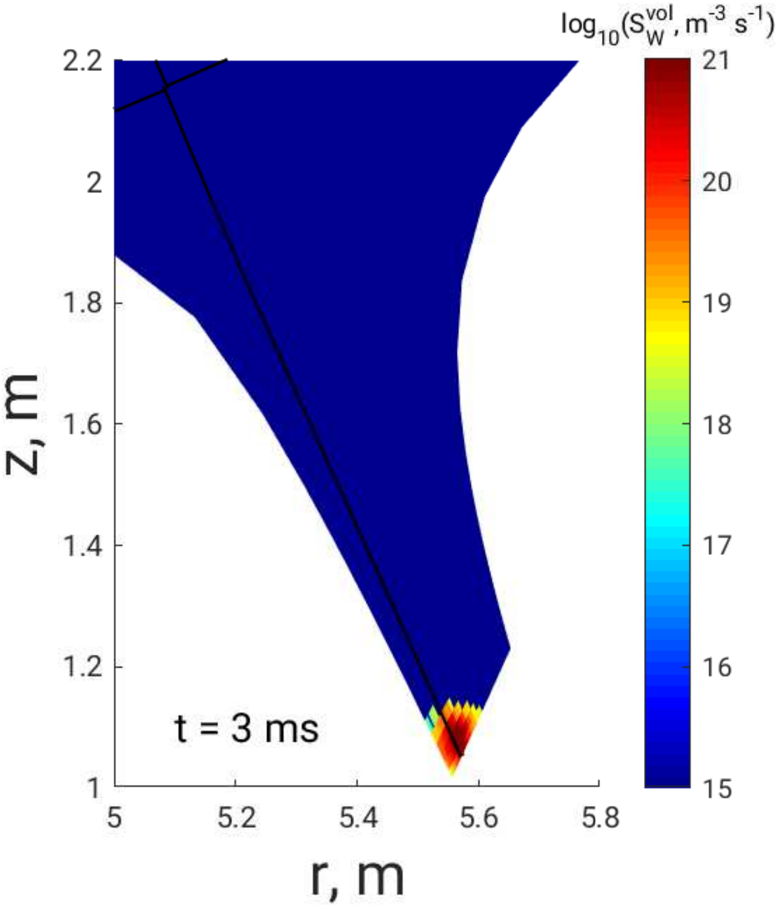
log$_{10}$(S$_W^{vol}$, m^{-3} s^{-1})
21
20
19
18
17
16
15
2.2
2
1.8
1.6
1.4
1.2
1
z, m
5
5.2
5.4
5.6
5.8
r, m
t = 3 ms

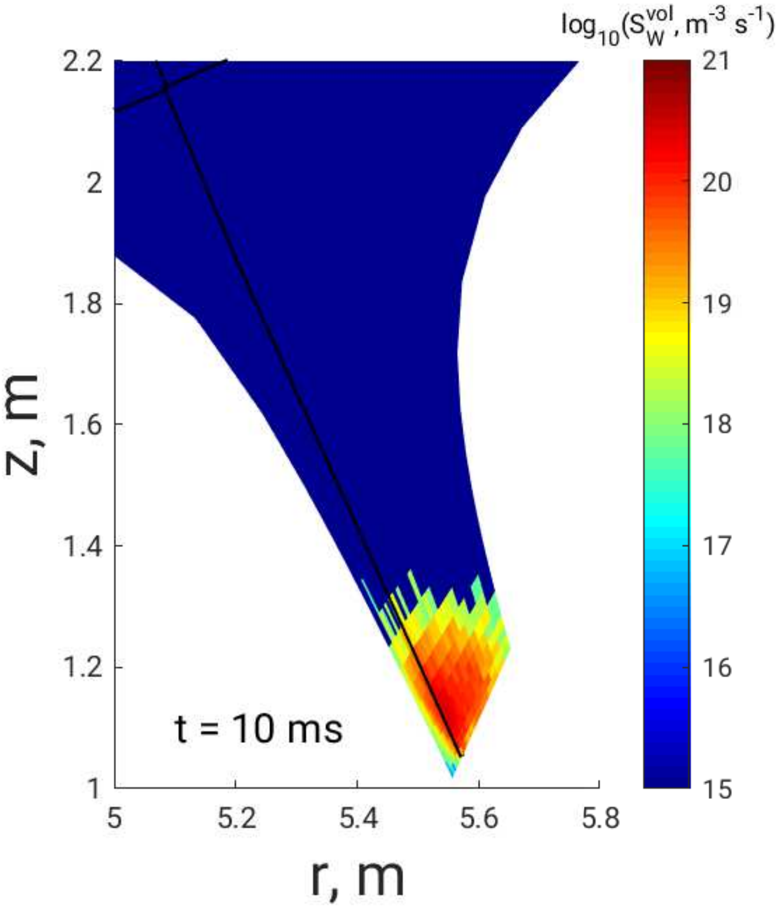
$\log_{10}(S_W^{vol}, m^{-3}\,s^{-1})$
21
20
19
18
17
16
15
2.2
2
1.8
1.6
1.4
1.2
1
z, m
5
5.2
5.4
5.6
5.8
r, m
t = 10 ms

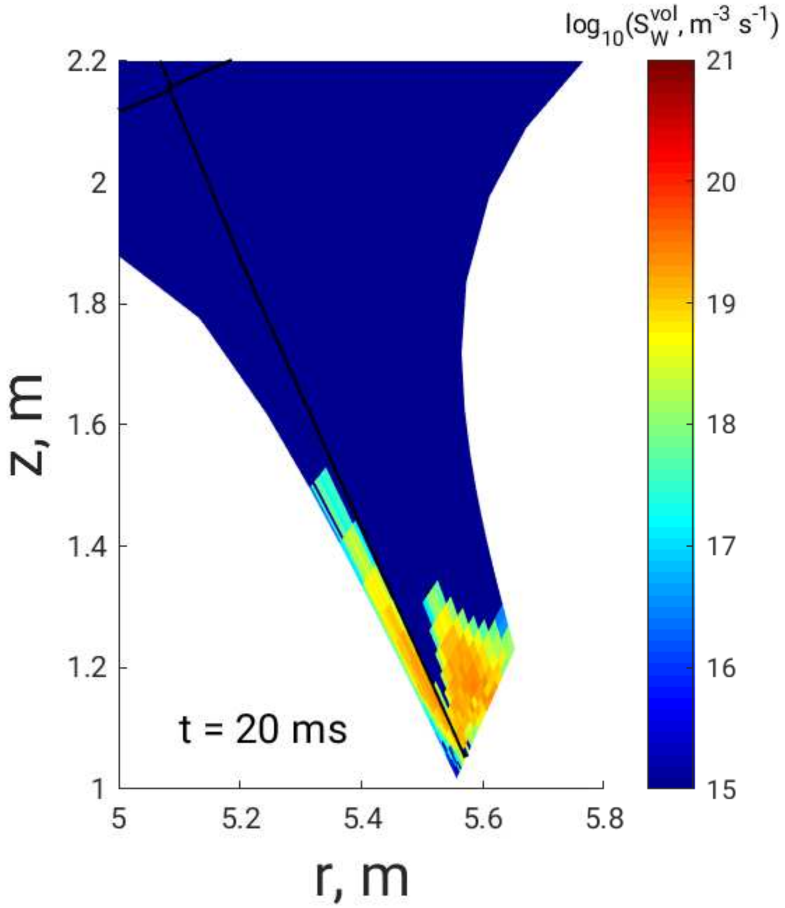
$\log_{10}(S_W^{vol}, m^{-3}\,s^{-1})$
21
20
19
18
17
16
15
2.2
2
1.8
1.6
1.4
1.2
1
z, m
5
5.2
5.4
5.6
5.8
r, m
t = 20 ms

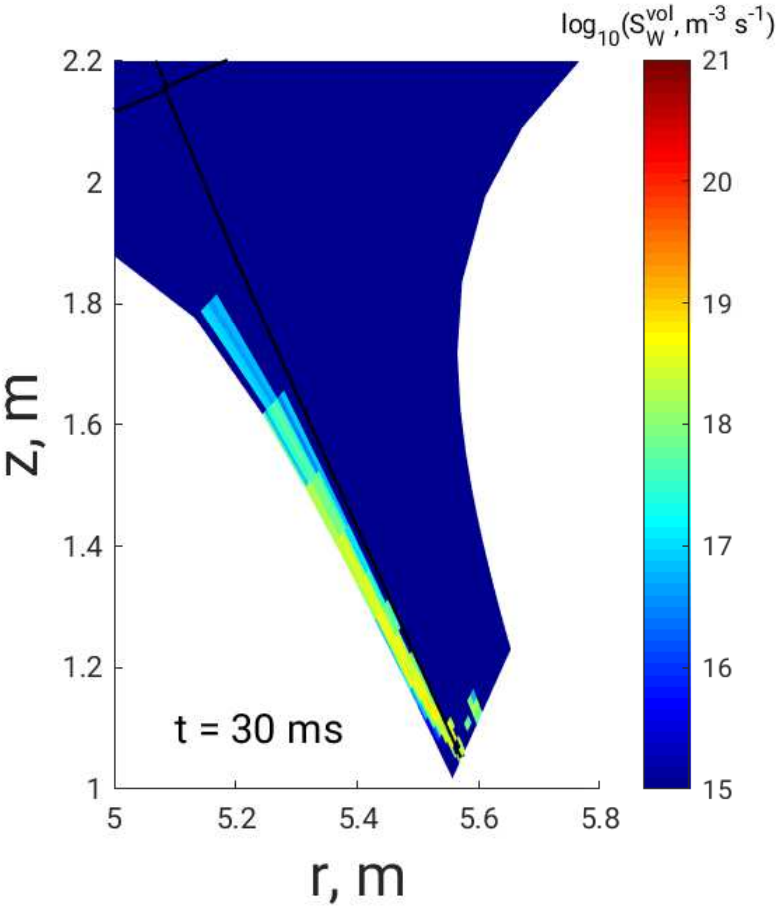
$\log_{10}(S_W^{vol}, m^{-3}\, s^{-1})$
21
20
19
18
17
16
15
t = 30 ms
z, m
2.2
2
1.8
1.6
1.4
1.2
1
r, m
5
5.2
5.4
5.6
5.8

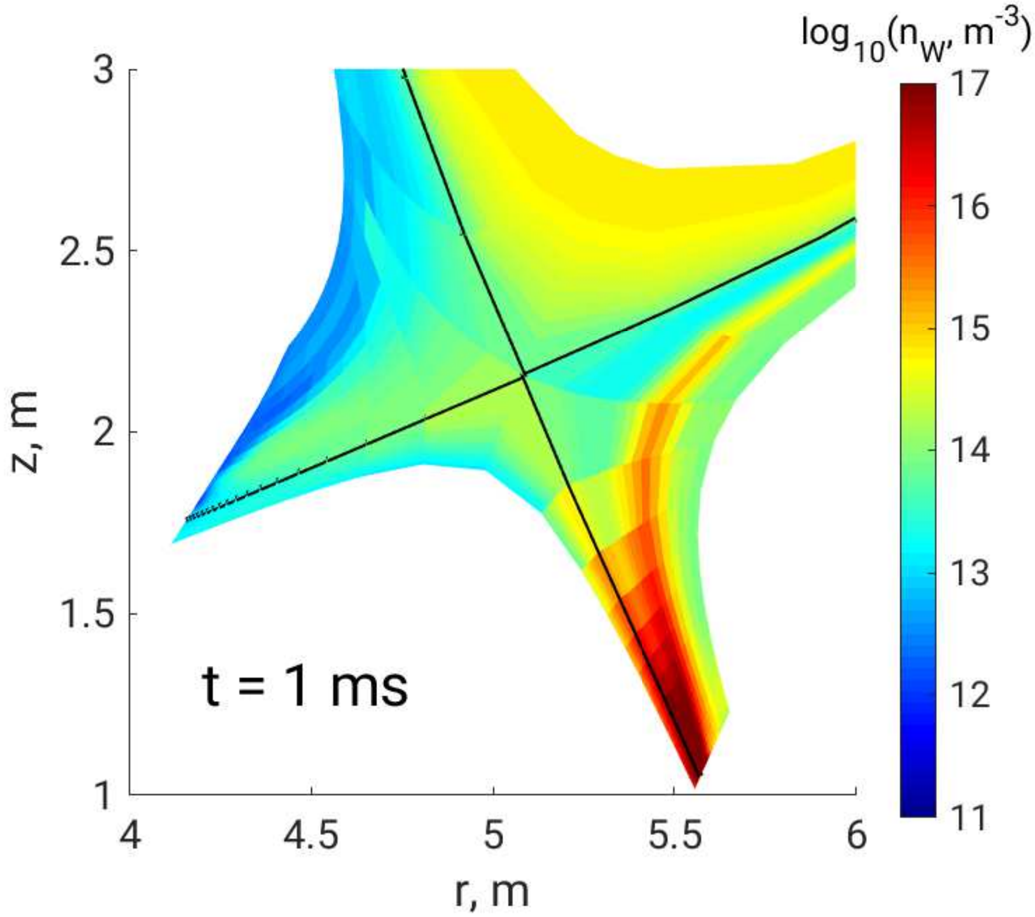
log$_{10}$(n$_W$, m^{-3})
17
16
15
14
13
12
11
z, m
3
2.5
2
1.5
1
r, m
4
4.5
5
5.5
6
t = 1 ms

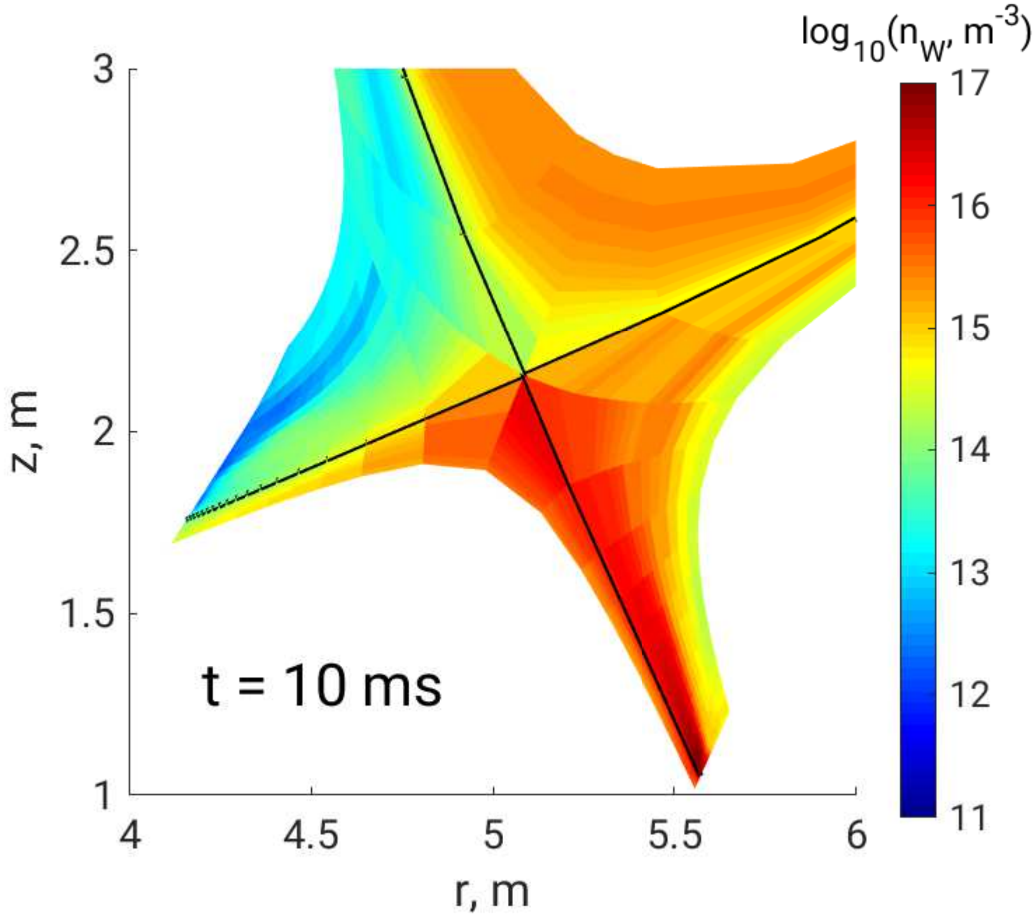
$\log_{10}(n_W, m^{-3})$
17
16
15
14
13
12
11
3
2.5
2
1.5
1
z, m
4
4.5
5
5.5
6
r, m
t = 10 ms

PLEASE CITE THIS ARTICLE AS DOI: 10.1063/5.0009767

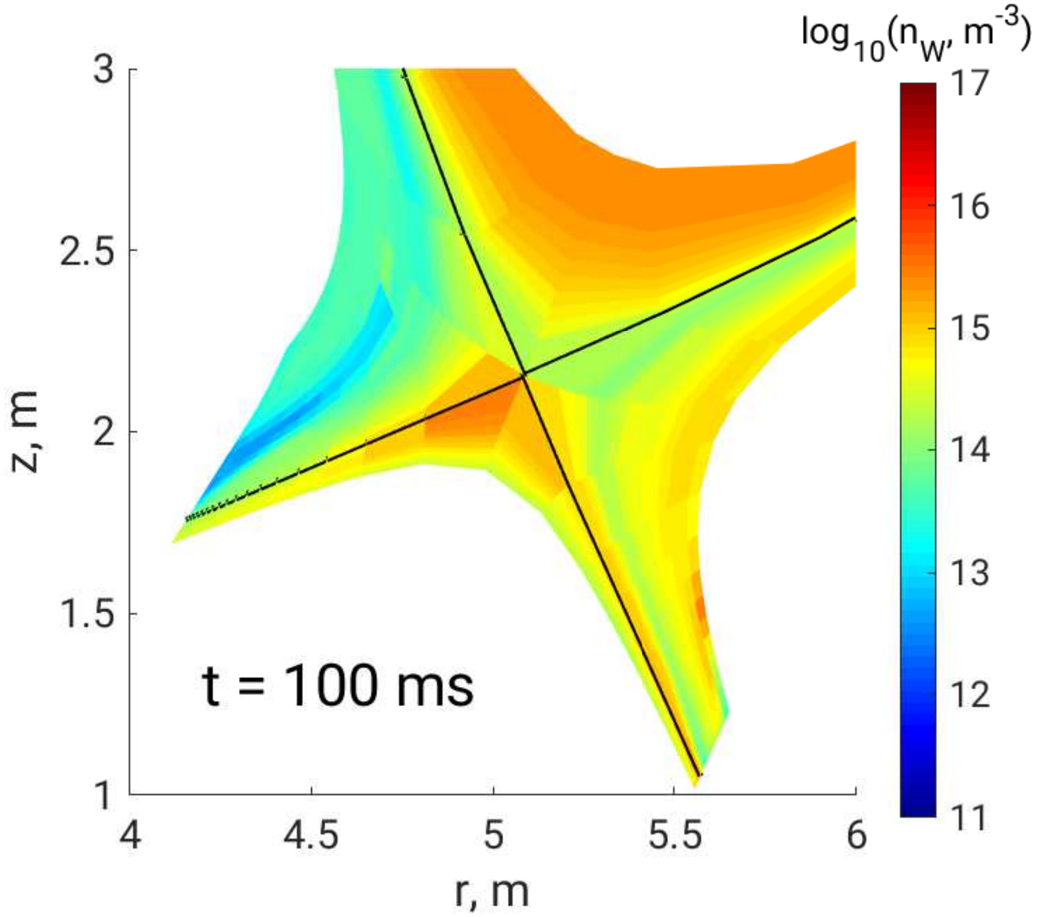

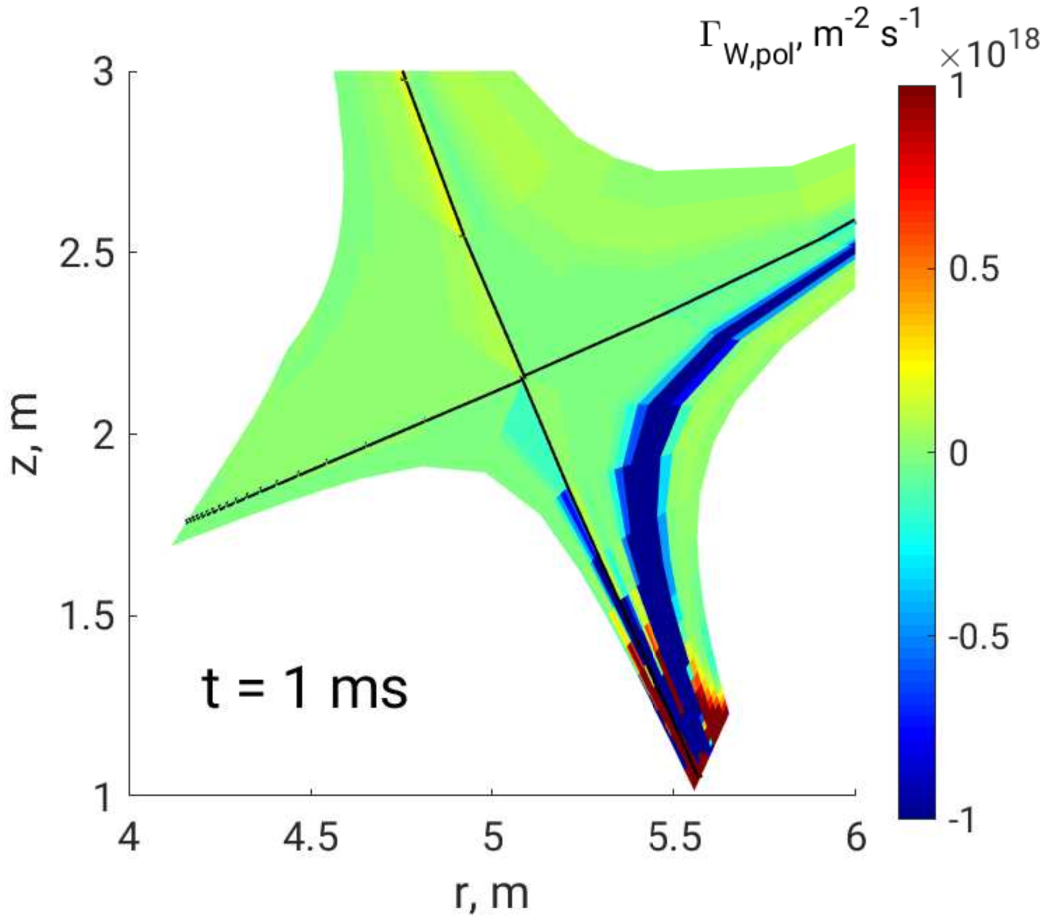
$\Gamma_{W,pol}$, m^{-2} s^{-1}
$\times 10^{18}$
1
0.5
0
-0.5
-1
3
2.5
2
1.5
1
z, m
4
4.5
5
5.5
6
r, m
t = 1 ms

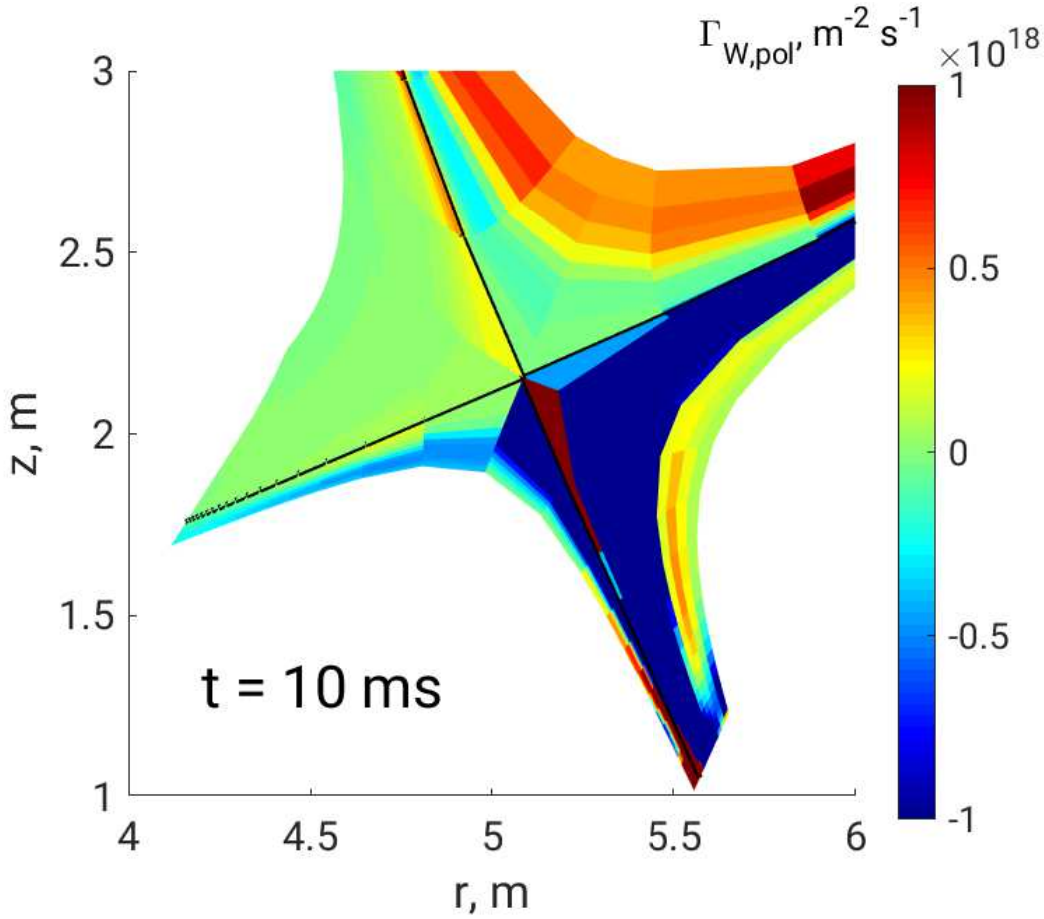
$\Gamma_{W,pol}$, m^{-2} s^{-1}
×10^{18}
1
0.5
0
-0.5
-1
3
2.5
2
1.5
1
z, m
4
4.5
5
5.5
6
r, m
t = 10 ms

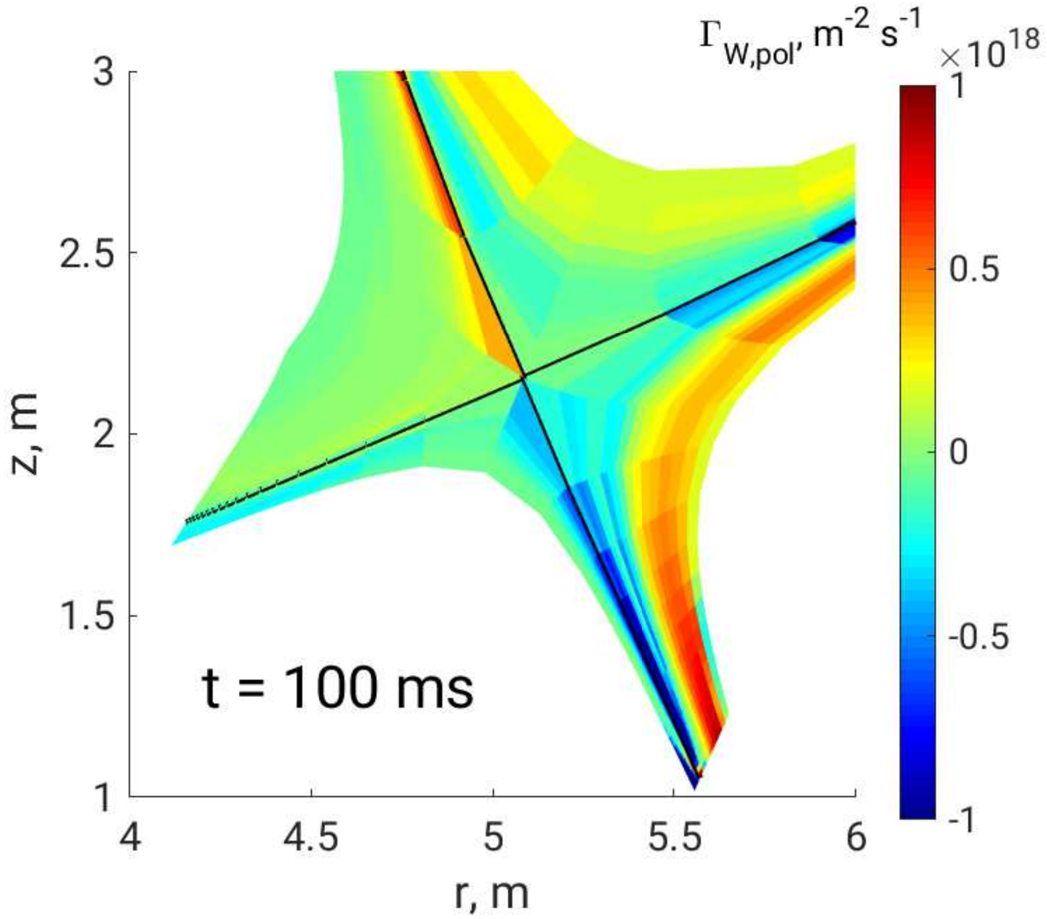
$\Gamma_{W,pol}$, m^{-2} s^{-1}
$\times 10^{18}$
1
0.5
0
-0.5
-1
3
2.5
2
1.5
1
z, m
4
4.5
5
5.5
6
r, m
t = 100 ms

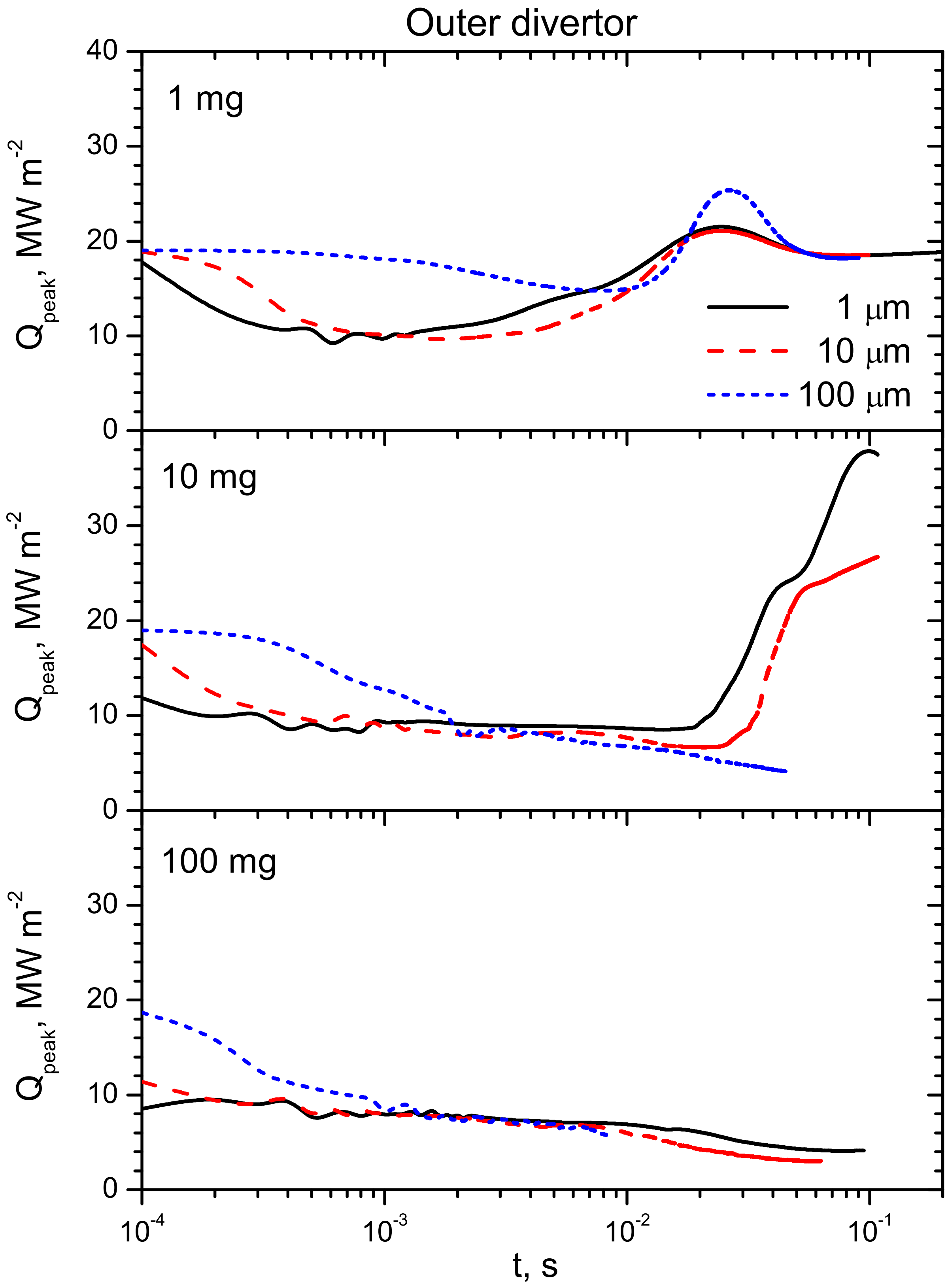
Outer divertor
1 mg
10 mg
100 mg
Q_{peak}, MW m^{-2}
0
10
20
30
40
1 μm
10 μm
100 μm
10^{-4}
10^{-3}
10^{-2}
10^{-1}
t, s

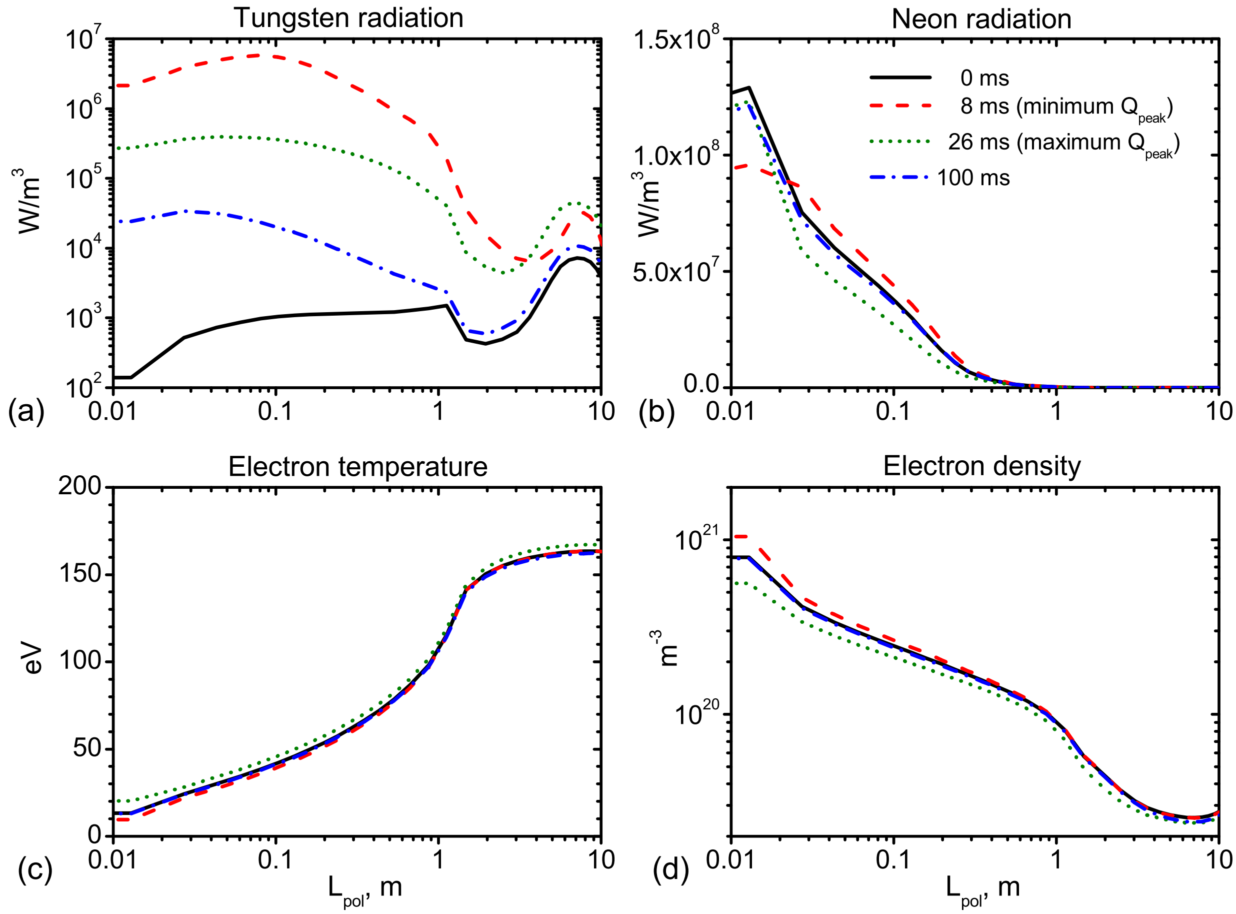
Tungsten radiation
10^7
10^6
10^5
10^4
10^3
10^2
W/m^3
(a)
0.01
0.1
1
10
Neon radiation
$1.5x10^8$
$1.0x10^8$
$5.0x10^7$
0.0
W/m^3
0 ms
8 ms (minimum Q_{peak})
26 ms (maximum Q_{peak})
100 ms
(b)
0.01
0.1
1
10
Electron temperature
200
150
100
50
0
eV
(c)
0.01
0.1
1
10
L_{pol}, m
Electron density
10^{21}
10^{20}
m^{-3}
(d)
0.01
0.1
1
10
L_{pol}, m

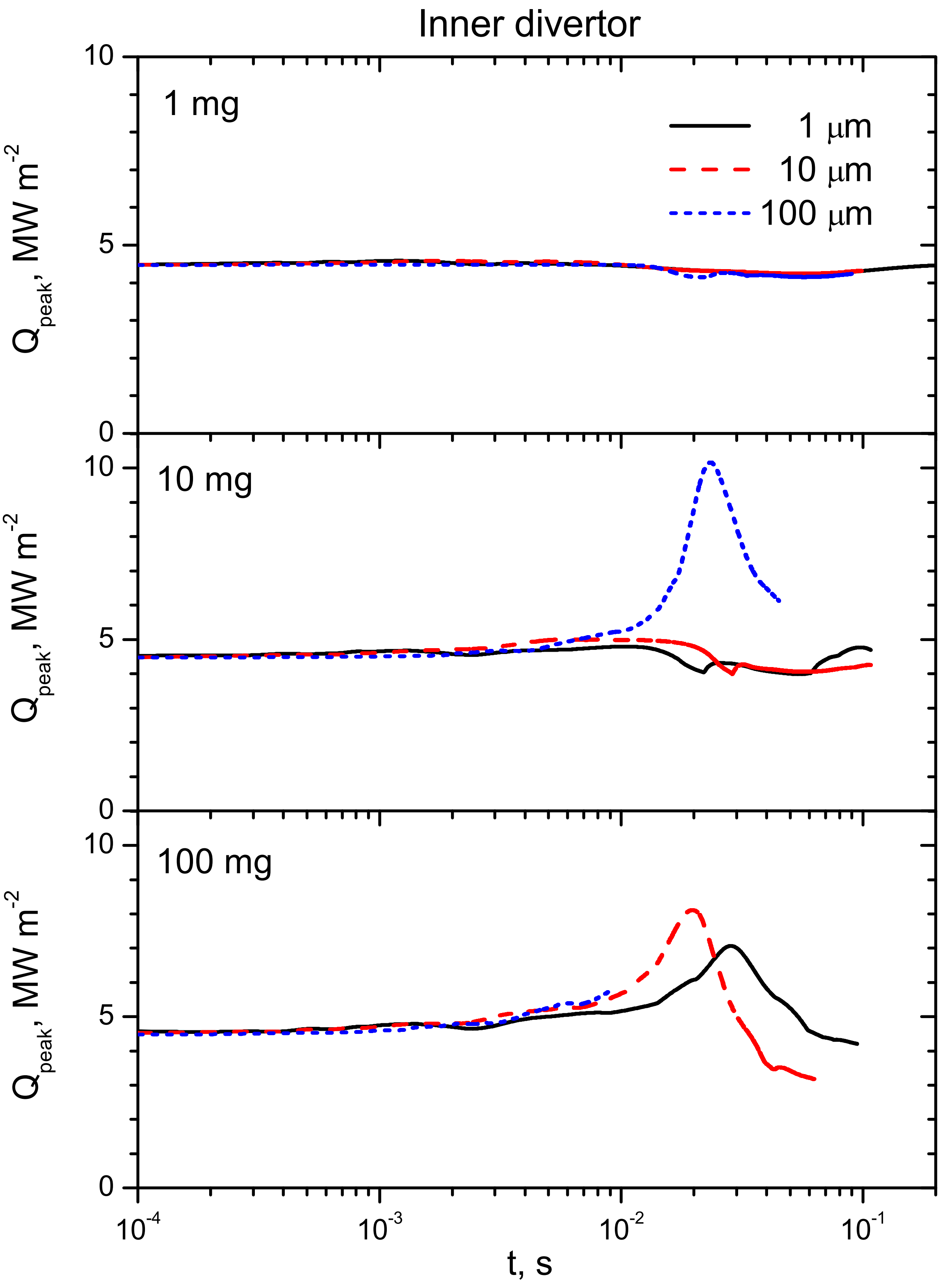
Inner divertor
1 mg
10 mg
100 mg
1 μm
10 μm
100 μm
Q_{peak}, MW m^{-2}
0
5
10
10^{-4}
10^{-3}
10^{-2}
10^{-1}
t, s

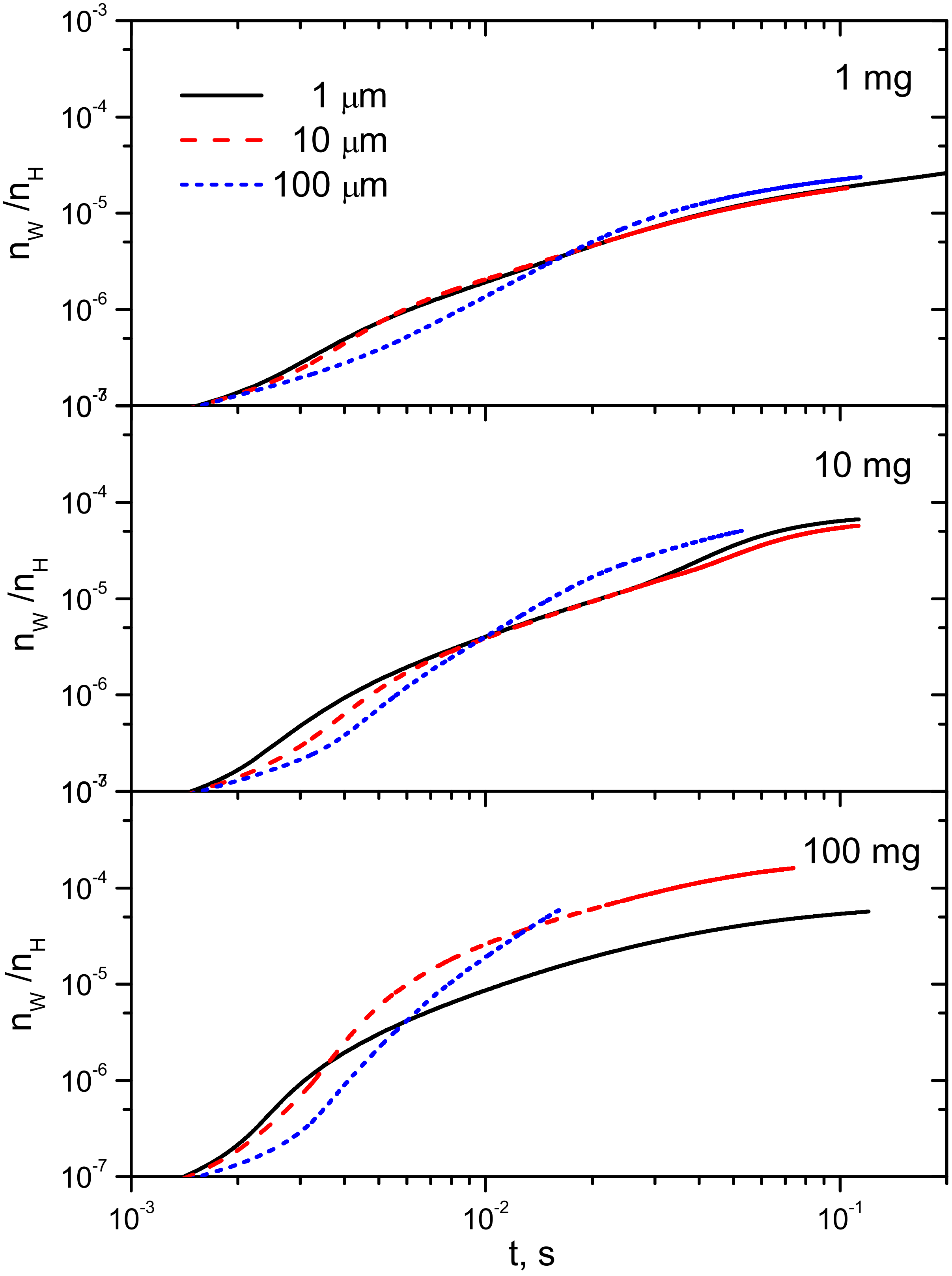
1 μm
10 μm
100 μm
1 mg
10 mg
100 mg
n_W/n_H
10^{-3}
10^{-4}
10^{-5}
10^{-6}
10^{-7}
10^{-3}
10^{-2}
10^{-1}
t, s